

# Measurement of all orthogonal components of displacement in the volume of scattering materials using Wavelength Scanning Interferometry

Semanti Chakraborty & Pablo D. Ruiz

Wolfson School of Mechanical & Manufacturing Engineering

Loughborough University, Loughborough, LE113TU, UK

## Abstract

A Wavelength Scanning Interferometry (WSI) system is proposed that provides displacement fields inside the volume of semi-transparent scattering materials with high spatial resolution and three-dimensional displacement sensitivity. This effectively extends Digital Speckle Pattern Interferometry into three dimensions. The sample is illuminated by three non-coplanar collimated beams around the observation direction. Sequences of two-dimensional interferograms are recorded whilst tuning the laser frequency at a constant rate. Different optical paths along each illumination direction ensure that the signals corresponding to each sensitivity vector do not overlap in the frequency domain. All the information required to reconstruct the location and the 3-D displacement vector of scattering points within the material is thus recorded simultaneously. A controlled validation experiment is performed, which confirms the ability of the technique to provide three dimensional displacement distributions inside semi-transparent scattering materials.

**Keywords:** wavelength scanning interferometry, frequency scanning interferometry, depth-resolved measurements, identification techniques, phase tomography, displacement tomography, strain tomography, digital speckle pattern interferometry.

## 1. Introduction

Experimental mechanics is currently contemplating tremendous opportunities of further advancements thanks to a combination of powerful computational techniques and also full-field non-contact methods to measure displacement and strain fields in a wide variety of materials. Identification techniques, aimed to evaluate material mechanical properties given known loads and measured displacement or strain fields, are bound to benefit from increased data availability (both in density and dimensionality) and efficient inversion methods such as Finite Element Updating (FEU) and the Virtual Fields Method (VFM) [1-3]. They work at their best when provided with dense and multicomponent experimental displacement (or strain) data, i.e. when all orthogonal components of displacements (or all components of the strain tensor) are known at points closely spaced ‘within’ the volume of the material under study. Although a very challenging requirement, an increasing number of techniques are emerging to provide such data. Techniques such as neutron diffraction and x-ray diffraction can provide 3-D strain fields in crystalline materials effectively measuring changes in the lattice parameter, but require long acquisition times for each measured point and rely on spatial scanning [4,5]. Digital volume correlation (DVC) [6,7] has gained popularity over the last few years for volumetric strain and displacement measurements. It effectively extends digital image correlation (DIC) and particle image velocimetry (PIV) [8], used from the early 1980’ to measure surface displacements and fluid flow. DVC has been used on data volumes acquired with a diverse range of techniques to evaluate 3-D deformation fields in a variety of materials, and some examples include: X-ray computed tomography (CT) of bones, sugar packs and silicon rubber phantoms [9-11]; scattered light imaging using sheet illumination in polymer phantoms [12]; ultrasound imaging of breast tumors [13]; confocal microscopic imaging of agarose gel phantoms [14]; Optical coherence

tomography (OCT) (also known as OCT elastography when combined with DIC or DVC) using 2-D cross correlation speckle tracking to compute deformation of gelatine scattering models, muscle tissue and skin [15]. In all these cases, spatial features which are part of the material microstructure are tracked to sub-pixel accuracy. Magnetic resonance imaging (MRI) has also been used to evaluate 3-D deformation inside bones and tendons [16,17] in conjunction with 2-D DIC. An alternative method based on high-resolution 3-D MRI volumes and a surface registration algorithm based on finite element optimization was used to evaluate the growth of cortical surfaces during the folding of cerebral cortex of human and animal brains [18]. Also, 3-D bulk displacements measured by stimulated echo MRI were used in conjunction with VFM to reconstruct the stiffness ratio between an inclusion and its surrounding medium in a phantom [19].

Tomographic photoelasticity relies on the retardation between different polarization components as light propagates through a transparent material that shows transient birefringence when loaded. It requires careful experimental measurements and inversion algorithms to retrieve all the components of the stress tensor [20]. Polarisation sensitive OCT also relies on the photoelastic effect to measure strains but it also provides depth-resolved distributions of birefringence, optical axis orientation and phase retardation due to tissue fibre orientation [21]. It is effectively a type of reflection mode photoelasticity that uses scattered light, with the ability to image structures and features within the volume of scattering materials. It provides the difference between the in-plane principal strain components.

A family of optical techniques has recently emerged, all of which can be considered as a type of phase-contrast OCT [22], also related to Doppler OCT [23]. They have the ability to measure displacement fields inside the volume of scattering materials without requiring birefringence, as

opposed to PSOCT or tomographic photoelasticity, and with interferometric sensitivity. These techniques include: 1) Wavelength scanning interferometry (WSI), which relies on a tunable laser. WSI systems with out-of-plane sensitivity were proposed to measure depth resolved displacements of a stack of optically smooth glass air interfaces [24] and also of scattering surfaces [25]; 2) Tilt scanning interferometry (TSI), in which a temporal sequence of monochromatic speckle interferograms is recorded while the illumination beam is tilted at a constant rate, was shown to provide 3-D displacement fields with one in-plane and out-of-plane sensitivity within an epoxy beam [26]; 3) Phase contrast spectral OCT (PC-SOCT) is based on a broadband source and spectral detection. A system was proposed to measure out-of-plane displacements in cross sections of porcine corneas due to changes in intra-ocular pressure [27] and also one in-plane and the out-of-plane components in cross sections of a polymer phantom [28]. Notice that in neither of these instances were all the components of the displacement field measured within the material volume. It is interesting to note that WSI, TSI and PC-SOCT can all be described in a common mathematical framework, as linear filters in 3-D space [29].

In this paper we describe a method to measure a 3-D displacement field within a semitransparent scattering material using WSI. All the components of the displacement vector are obtained in each voxel of the data volume. This is achieved by simultaneously measuring the interference signal produced for different illumination directions during a wavelength scan. These are separated in the frequency domain by adjusting the optical path difference between the illumination and reference beams, thus introducing different carrier frequencies to the interference signal for different illumination direction. In Section 2 the Optical setup is described. In Section 3 we describe the principle of WSI, the new approach based on frequency multiplexing, and the main elements of the mathematical framework for WSI. In Section 4, data

acquired for a reference opaque surface is used to evaluate the sensitivity vectors of the interferometer, rather than establishing them from approximate illumination and observation directions measured from the setup. The relationship between measured phase and calculated displacements is thus established in a convenient reference system. In Section 5 we present experimental results of the 3-D distribution of the displacement field within a test sample that has undergone known rigid body in-plane rotation and out-of-plane tilt. All the components of the displacement vector at each voxel of the data volume are measured and compared to the nominal values of rotation and tilt introduced in the experiment via two rotation and tilt stages. Finally, in Section 6 we present a discussion on potential applications, sources of error and opportunities for further refinement and we derive some conclusions.

## 2. Optical setup

Fig. 1 shows a top view of the optical setup. The light source consists in a tunable laser, TL, (TSL-510 Type A, Santec Ltd.) which can scan the wavelength from 1260 to 1360 nm in steps as small as 0.011 nm. This corresponds to a frequency scan from 237.9305 to 220.4356 THz with a 0.002 THz frequency step. The laser is connected via a single mode optical fibre (SMF) to a 2×4 fibre optic splitter (Shenzhen gigalight, planar lightwave circuit (PLC), wavelength range 1260-1650 nm, SMF) that divides power equally between the four output channels into SMF fibres (the second input channel is not used). One output channel, OF<sub>R</sub>, feeds the reference arm of the interferometer whilst the other three, OF<sub>1</sub>, OF<sub>2</sub> and OF<sub>3</sub>, provide three illumination beams. These are collimated by near-infrared double achromats L<sub>1</sub>, L<sub>2</sub> and L<sub>3</sub> and arranged so that they illuminate the sample, S, from three non-co-planar directions. The beams subtend zenith angles  $\theta_1$ ,  $\theta_2$  and  $\theta_3$  to the optical axis of the imaging system formed by lenses L<sub>6</sub> and L<sub>7</sub> and are

arranged symmetrically around it with azimuth angles  $\xi_1$ ,  $\xi_2$  and  $\xi_3$  as shown in the insert in Fig. 1. Upon scattering on sample S, reference and object beams are combined with a 45:55 pellicle beam splitter (PBS) and detected with a near-infrared InGaAs photodetector array (SU640SDV-1.7RT/RS170, Goodrich Corporation, 640×512 pixels, 14 bit). Lenses  $L_6$  and  $L_7$  form a ‘ $4f$ ’ double telecentric imaging system. An aperture stop (AS) serves to control telecentricity, speckle size and throughput. In the reference beam, a pinhole, PH, is used as a spatial filter and also to control the intensity ratio between reference and object beams.

A critical detail in this setup is the way in which the optical path lengths are adjusted for the reference and object beams. The reference beam optical path is adjusted with a delay line, while those of the object beams are adjusted by positioning collimating lenses  $L_1$ ,  $L_2$  and  $L_3$  at slightly different distances from the sample. If we consider a sphere centred at the intersection between the sample surface and the optical axis of the imaging system, then the optical centre of  $L_1$  lies within the sphere, of  $L_2$  on the sphere surface and of  $L_3$  outside it. If we assume equal optical paths within the optical fibres  $OF_1$ ,  $OF_2$  and  $OF_3$  then the distances from the collimating lenses to the sphere determine their relative optical path differences, which are used to separate information from different sensitivity directions in the frequency domain. This is described in detail in the next Section. The setup described above is effectively a Mach-Zehnder interferometer with multiple illumination directions that are frequency multiplexed by offsetting their optical path delays.

### **3. Full-sensitivity phase-contrast Wavelength Scanning Interferometry**

#### **3.1 Working Principle**

Consider a plate made of a semi-transparent scattering material that is illuminated and observed using the interferometer shown in Fig. 1. The observation direction is defined as the  $z$ -axis. The plate's surface is imaged on the photodetector array with magnification  $M=1$ . The  $z$ -component of points represented by position vectors  $\mathbf{r}_s$  and  $\mathbf{r}$  measures the distance between the reference wavefront and the surface and a point within the material, respectively. A detailed ray diagram is shown in Fig. 2(a) for one illumination beam on the plane of incidence. A point with coordinates  $\mathbf{r}=(x, y, z)$  in the material is imaged onto a pixel with indices  $(m, n)$  of the photodetector array.  $p_x, p_y$  are defined respectively as the pitch between pixels along the  $n$  and  $m$  axes on the photodetector array so that  $x=np_x$  and  $y=mp_y$ . The optical path difference between light from the  $p$ -th illumination beam scattered at point  $(x, y, z)$  within the material and the reference wave can be written as

$$\Lambda_p(x, y, z) = n_0[\mathbf{e}_p \cdot (\mathbf{r}_0 - \mathbf{r}_p) + \mathbf{e}_p \cdot (\mathbf{r}_e - \mathbf{r}_0)] + n_1[\mathbf{e}_{p'} \cdot (\mathbf{r} - \mathbf{r}_e) + \mathbf{e}_o \cdot (\mathbf{r}_s - \mathbf{r})] + n_0\mathbf{e}_o \cdot \mathbf{r}_s \quad (1)$$

$n_0$  and  $n_1$  are the refractive indexes of the surrounding medium (air in this case) and the material, respectively.  $\mathbf{e}_p, \mathbf{e}_{p'}$  and  $\mathbf{e}_o=(0,0,-1)$  are unit vectors along the  $p$ -th illumination direction within the surrounding medium, the illumination direction within the material, and the observation direction, respectively.  $\mathbf{r}, \mathbf{r}_0, \mathbf{r}_e, \mathbf{r}_s$  and  $\mathbf{r}_p$  are respectively the position vectors of points  $(x, y, z)$  within the material, imaged onto pixel  $(m, n)$ ;  $(x_0, y_0, z_0)$  which is imaged onto pixel  $(0, 0)$ ;  $(x_e, y_e, z_e)$  where light reaching point  $\mathbf{r}$  in the material is refracted at the surface;  $(x_s, y_s, z_s)$  on the material's surface which is also imaged onto pixel  $(m, n)$ ; and finally of  $(x_p, y_p, z_p)$  which locates a point on the illumination wavefront propagating with direction  $\mathbf{e}_p$  that reaches the object at  $\mathbf{r}_0$ . The triangle with  $r_e-r_0$  as the hypotenuse is a right triangle, and all incoming vectors are parallel. The first term on the RHS of Eqn. (1) represents the optical path from a point on the illumination wavefront,  $\mathbf{r}_p$ , to point  $\mathbf{r}_e$ , where light enters the material. The second term represents the optical

path due to propagation within the material upon refraction, from point  $\mathbf{r}_e$  to  $\mathbf{r}$  and back to the surface at  $\mathbf{r}_s$ . Finally, the last term represents the optical path from the object surface at  $\mathbf{r}_s$  to the reference beam's zero delay wavefront at  $z=0$ .

The relationship between  $\mathbf{r}_s$  and  $\mathbf{r}_e$  in a general case is governed by refraction at  $\mathbf{r}_e$  by

$$|\mathbf{r}_s - \mathbf{r}_e| = |\mathbf{r} - \mathbf{r}_s| \tan(\theta_{p'}) \quad (2)$$

and the Snell's law in vector form:

$$n_0(\mathbf{N} \times \mathbf{e}_p) = n_1(\mathbf{N} \times \mathbf{e}_{p'}) \quad (3)$$

where  $\theta_p$  and  $\theta_{p'}$  are the incidence and refracted angles of the  $p$ -th beam,  $\mathbf{N}$  is a unit vector normal to the surface,  $(0, 0, 1)$  here, and  $\mathbf{e}_{p'}$  is a unit vector pointing along the refracted beam.

This vector representation is convenient when dealing with non-coplanar illumination and observation directions, especially at the data processing stage. In the following analysis, we will consider the case of a flat sample that lies perpendicular to the observation direction to eliminate extra terms that would appear due to refraction at the surface. The general case is described in Section 2.3.1.4 in [30].

It is convenient to model the object as a set of  $N_s$  discrete thin scattering layers parallel to its surface. The intensity due to the interference of the three object wavefronts and the reference wavefront can be written as

$$I(m, n, t) = |A_0(m, n, t) + \sum_{p=1}^3 \sum_{j=1}^{N_s} A_{pj}(m, n, t) \exp[i\phi_{pj}(m, n, t)]|^2 \quad (4)$$

$A_0$  represents the amplitude of the reference wavefront.  $A_{pj}$  ( $p=1, 2, 3; j=1, 2, \dots, N_s$ ) is the amplitude of the wavefront scattered at the  $j$ -th slice when illuminated by the  $p$ -th beam.  $\phi_{pj}$  is the phase difference between light scattered at the  $j$ -th slice when illuminated by the  $p$ -th beam and the reference beam. The spatial indices  $m$  and  $n$  take the values  $m = 0, 1, 2, \dots, N_m-1; n = 0, 1, 2,$

...,  $N_n-1$  and  $t$  is a non-dimensional time defined as the true time divided by the camera interframe time. Expanding Eqn. (4) and dropping the  $(m, n, t)$  dependence in all the amplitude and phase variables for clarity gives

$$I(m, n, t) = A_0^2 + \sum_{p=1}^3 \sum_{j=1}^{N_s} A_{pj}^2 + 2 \sum_{p=1}^2 \sum_{q=p+1}^3 \sum_{j=1}^{N_s-1} \sum_{k=j+1}^{N_s} A_{pj} A_{qk} \cos(\phi_{pj} - \phi_{qk}) + 2 A_0 \sum_{p=1}^3 \sum_{j=1}^{N_s} A_{pj} \cos \phi_{pj} \quad (5)$$

The right hand side of Eqn. (5) consists of four terms. The first two correspond to a slowly varying function of time due to both the envelope of the tunable laser power spectrum and to the wavelength dependence of the scattered amplitude. Term 3 represents interference between the light from the  $j$ -th and the light from the  $k$ -th layers corresponding to either the same or different illumination beams indicated by indexes  $p$  and  $q$ , and together with Term 2 are referred to as the autocorrelation terms (AC). Term 4 represents the interference between the scattered light from the  $j$ -th slice when illuminated by the  $p$ -th beam and the reference beam, and is referred to as the cross correlation term (CC). This latter term contains the information about the microstructure of the sample.

The phase  $\phi_p$  changes with time according to

$$\phi_{pj}(m, n, t) = \phi_{sj}(m, n) + k(t) \Lambda_{pj}(m, n), \quad (6)$$

where  $k(t)$  is the wavenumber  $2\pi/\lambda(t)$ , and  $\phi_{sj}$  is a phase shift that may arise at zero nominal path difference due to, for instance, a phase change on reflection or due to the microscopically random arrangements of scatterers contributing to the amplitude at pixel  $(m, n)$  at the  $j$ -th slice, i.e. the phase that leads to speckle noise.  $\Lambda_{pj}$  represents the optical path difference given in Eqn. (1) due to the  $p$ -th beam and for the  $j$ -th slice, which lies at a depth  $z=z_0+(j-1/2)\delta z$  below the

sample's surface,  $\delta z$  being the layer thickness. WSI involves changing  $k$  with time over a total range  $\Delta k$  while an image sequence is recorded. In the ideal case of a linear variation of  $k$  with  $t$ ,

$$k(t) = k_c + \delta k t \quad (7)$$

Where  $k_c$  is the central wavenumber,  $\delta k$  is the interframe wavenumber increment and  $t$  ranges from  $-\Delta k/2\delta k$  to  $+\Delta k/2\delta k$ . Substitution of Eqn. (7) into Eqn. (6) leads to

$$\phi_{pj}(m, n, t) = \phi_{sj}(m, n) + k_c \Lambda_{pj}(m, n) + \delta k \Lambda_{pj}(m, n) t, \quad (8)$$

The linear variation of  $\phi_{pj}$  with  $t$  leads to temporal frequencies (units of ‘‘cycles per frame’’)

$$f_{\Lambda_{pj}}(m, n) = \delta k \Lambda_{pj}(m, n) / 2\pi, \quad (9)$$

that is, frequencies proportional to the optical path difference between light from the  $p$ -th beam scattered at the  $j$ -th layer and the reference wavefront. It is convenient to define an alternative frequency in units of ‘‘cycles per scan duration’’

$$\hat{f}_{\Lambda_{pj}}(m, n) = f_{\Lambda_{pj}} N_t = \Delta k \Lambda_{pj}(m, n) / 2\pi, \quad (10)$$

Thus, measuring frequencies  $f_{\Lambda_{pj}}$  or  $\hat{f}_{\Lambda_{pj}}$  in a pixel wise basis provides a measure of  $\Lambda_{pj}(m, n)$ , which can be used to locate the coordinates of scatterers on the surface and the bulk of the sample. Moreover, if two scans are performed before and after a deformation of the sample, then provided  $\phi_{sj}$  remains the same between scans, the phase changes  $\Delta \phi_{pj}(m, n, 0)$  provide a direct measure of the change in optical path lengths  $\Delta \Lambda_{pj}(m, n)$  due to the deformation.

Both the position and phase change of surface scatterers can be evaluated by a time-frequency analysis. The Fourier transform of the interference intensity signal  $I(m, n, t)$  in Eqn. (5) can be written as an infinite sum over an integer index that locates identical spectra  $N_t$  samples apart in the frequency domain. The goal of the measurement is to reconstruct the amplitude  $A_{pj}(m, n)$  and the phase  $\phi_{pj}(m, n)$  3-D distributions of the scattered light field from each of the  $N_s$  scattering

layers. If no aliasing is present, then the Fourier transform of the intensity in Eqn. (4) may be written as

$$\tilde{I}(\hat{f}) = \tilde{W}(\hat{f}) * \left\{ \begin{aligned} & \left( I_0 + \sum_{p=1}^3 \sum_{j=1}^{N_s} I_{pj} \right) \delta(\hat{f}) + \sum_{p=1}^3 \sum_{j=1}^{N_s} \sqrt{I_0 I_{pj}} \exp(\pm i \phi_{0pj}) \delta(\hat{f} \mp \hat{f}_{\Lambda pj}) \\ & + \sum_{p=1}^2 \sum_{q=p+1}^3 \sum_{j=1}^{N_s-1} \sum_{k=j+1}^{N_s} \sqrt{I_{pj} I_{qk}} \exp[\pm i(\phi_{0pj} - \phi_{0qk})] \delta[\hat{f} \mp (\hat{f}_{\Lambda pj} - \hat{f}_{\Lambda qk})] \end{aligned} \right\} \quad (11)$$

where \* represents convolution,  $\tilde{W}(\hat{f})$  is the Fourier transform of  $W(t)$ , a continuous window function that represents the finite sampling duration and the envelope of the laser power spectrum. The first term between curly brackets in Eqn. (11) represents the DC term due to the reference and scattered wavefronts. The second, known as the cross-correlation term, represents the interference between the reference and all three illumination beams scattered at all layers within the sample and is given by the superposition of Dirac deltas  $\delta$  that fall within bands in the frequency domain between frequencies  $\hat{f}_{\Lambda p1}$  and  $\hat{f}_{\Lambda pN_s}$  which are, according to Eqn. (10), proportional to the optical paths  $\Lambda_{p1}$  and  $\Lambda_{pN_s}$  corresponding to the first and last layers. The phase at the origin of each of these frequency components is given by  $\phi_{0pj} = \phi_{pj}(m, n, 0)$ . The third term, known as autocorrelation, represents the interference between pairs of scattering layers corresponding to either the same illumination beam or different ones. It is represented by Dirac deltas at frequencies  $\pm(\hat{f}_{\Lambda pj} - \hat{f}_{\Lambda qk})$ . In order for all the cross correlation frequency bands to be fully separated in the frequency domain and avoid overlap with the autocorrelation terms, the carrier frequencies  $\hat{f}_{\Lambda pj}$  and  $(\hat{f}_{\Lambda pj} - \hat{f}_{\Lambda qk})$  must be carefully set. This is done by adjusting the optical paths  $\Lambda_{pj}$  by moving the collimating lenses  $L_1$ ,  $L_2$  and  $L_3$ , which will shift the wavefront

represented in Eqn. (1) by position vector  $\mathbf{r}_p$ . The second term in Eqn. (1) thus adjusts a ‘piston’ term in the optical path difference  $\Lambda_{pj}$  and is characteristic of each illumination beam.

### 3.2 Range and resolution of the optical path difference measurement

The maximum unambiguous range that the optical path difference may take is given by the Shannon sampling theorem, which states that in order to ensure adequate sampling of the  $I(m, n, t)$  signal, the phase difference  $\phi_{pj}$  should not change by more than  $\pi$  between successive  $t$  values, i.e. 2 samples per cycle. This leads to a maximum allowed optical path difference

$$\Lambda_M = \frac{\pi}{\delta k}. \quad (12)$$

The resolution to which the optical path length may be measured can be characterized by the width of the peaks in the Fourier domain, given by the width of  $\tilde{W}(\hat{f})$ . A usual resolution criterion is a frequency difference between two neighbouring peaks of at least twice the distance from their centres to their first zero. For the case of normal observation with a telecentric system as the one illustrated in Fig. 2, the width of the spectral peak and hence the optical path resolution can be written as

$$\delta\Lambda = \gamma \frac{2\pi}{N_t \delta k}, \quad (13)$$

in the case of a scattering point in air, and

$$\delta\Lambda = \gamma \frac{\pi}{n_1 \cos(\theta_p / 2) N_t \delta k}, \quad (14)$$

in the case of scattering points within a medium of refractive index  $n_1$ . We are assuming a plane air/medium interface at which refraction occurs,  $\theta_p$  is the refracted angle and the constant  $\gamma$  takes the value 2 for a rectangular window and 4 for a Hanning window, for example

#### 4. Image reconstruction performance

A flat scattering surface (sandblasted Aluminium plate) was first studied using the interferometer shown in Fig. 1. The purpose of this was to assess the performance of the laser and the NIR camera in terms of the linearity of the wavenumber scan  $k(t)$  and the intensity noise, which ultimately determine the width of the peak that represents the surface in the Fourier transform  $\tilde{I}(\hat{f})$ , i.e. the optical path resolution  $\delta\lambda$ . This is presented in Section 4.1.

Furthermore, it turns out that the scattering surface appears tilted due to the oblique illumination beams that introduce a linear spatial variation of the optical path difference in Eqn. (1), which in the case of a scattering surface reduces to

$$\Lambda_p(x, y, z) = n_0[\mathbf{e}_p \cdot (\mathbf{r}_0 - \mathbf{r}_p) + \mathbf{e}_p \cdot (\mathbf{r} - \mathbf{r}_0) + \mathbf{e}_o \cdot \mathbf{r}] \quad (15)$$

with  $\mathbf{r}$  the position vector of point  $(x, y, z)$  now representing a point on the surface - see Fig. 2(b). As the orientation of these tilted planes in the frequency domain is directly related to the orientation of the illumination beams, they can be conveniently used to calculate the illumination unit vectors  $\mathbf{e}_p$  shown in Fig. 1 and therefore the sensitivity vectors that link measured phase changes to actual 3-D displacement fields. This is described in Sections 4.2 and 4.3.

##### 4.1 Depth range and depth resolution

A sequence of 8748 frames was recorded during a laser frequency scan from  $\nu_1 = 237.9305$  THz to  $\nu_2 = 220.4356$  THz ( $\nu = c/\lambda = ck/2\pi$ , with  $c$  the speed of light in vacuum). Each frame was  $64 \times 64$  pixels, encoding the intensity  $I(m, n, t)$  in 14 bits. The field of view was ultimately limited by the random access memory available for data processing, but  $512 \times 640$  pixels (rows, columns) images can be acquired with the NIR camera. Fourier transformation of the recorded 3-D intensity distribution is performed on a pixel wise basis along the  $t$ -axis, leading to a spectrum

that is directly related to the position of the surface along the observation direction at coordinates  $x=np_x, y=mp_y$ . The tunable laser delivers a nearly constant power during the whole scan, which translates in a good level of signal modulation. Fig. 3(a) shows the intensity for a pixel at the centre, plotted against frame number, i.e.  $I(32, 32, t)$ . The mean value of the intensity signal was subtracted to eliminate the dominant DC peak at  $f_{\Lambda_p}=0$ . Also, the intensity signal was multiplied by a Hanning window  $W(t) = 0.5\{1 - \cos[2\pi(t + N_t/2)/N_t]\}$ ,  $-N_t/2 \leq t \leq +N_t/2$  to reduce spectral leakage between the otherwise prominent secondary lobes of a rectangular window  $\tilde{W}(\hat{f})$ . The Fourier transform of the signal in Fig. 3(a) is shown in Fig. 3(b) in the positive frequency axis and reveals six peaks. The frequency axis was converted to optical path difference by using Eqn. (10) and by noting that the optical path  $\Lambda_p$ . Peaks are labelled according to which pair of beams interfere; for instance, “01” indicates interference between the reference beam and object beam 1 and “23” indicates interference between object beams 2 and 3 (see insert in Fig.1). Notice in Fig. 3(b) how peaks “01”, “02”, “03” are fully separated. This separation is adjusted by moving lenses  $L_1, L_2$  and  $L_3$  towards or away from the sample so that the peaks do not overlap with the cross interference ones and no aliasing is introduced. Fig. 3(c) shows peak “01” in more detail. It has a width of  $\sim 0.06$  mm, which compares well with the expected value of 0.068 mm from Eqn. (13).

When this computation is done for every pixel and the cross interference between the object beams are neglected, an instance of the surface emerges for each object beam within the so-called ‘reconstruction volume’ in the ‘direct’, i.e.  $(x, y, z)$ , space. As mentioned before, the surface appears with different tilts for each illumination direction. Fig. 4 shows a slice through the reconstructed volume parallel to the  $yz$  plane for  $x=32$ . The three lines to the left correspond to the cross interference between the object beams. The three on the right correspond to the

interference between the object beams and the reference beam, and thus represent the object as reconstructed for each illumination direction.

#### 4.2 Evaluation of illumination and sensitivity vectors.

The tilt of the reconstructed surface is uniquely related to the illumination directions. This allows us to use them to calculate the orientation of the illumination beams  $\mathbf{e}_p$ . Fig. 5(a) shows the planes of best fit for all surface reconstructions “01”, “02” and “03”. The normal to reconstruction “01”, calculated from the coefficients of the plane of best fit, is shown in Fig. 5(b). It is convenient to denote the normal vector to the  $p$ -th reconstructed surface by  $\mathbf{n}_p$ , and express it in terms of  $\alpha_p$  and  $\beta_p$ , the zenith and azimuth angles that  $\mathbf{n}_p$  subtends from the observation axis and the  $x$ -axis, respectively. It can be shown that:

$$\mathbf{n}_p = (\sin \alpha_p \cos \beta_p, \sin \alpha_p \sin \beta_p, \cos \alpha_p) \quad (16)$$

or equivalently:

$$\alpha_p = \cos^{-1}(\hat{\mathbf{k}} \cdot \mathbf{n}_p) \quad (17)$$

$$\beta_p = \tan^{-1}\left(\frac{\hat{\mathbf{j}} \cdot \mathbf{n}_p}{\hat{\mathbf{i}} \cdot \mathbf{n}_p}\right) \quad (18)$$

$\hat{\mathbf{i}}$ ,  $\hat{\mathbf{j}}$  and  $\hat{\mathbf{k}}$  are unit vectors along the  $x$ ,  $y$  and  $z$  axes, respectively.

From Fig. 2(b) it follows that the optical path difference between points  $\mathbf{r}_0$  and  $\mathbf{r}$  is  $\Lambda(\mathbf{r}) - \Lambda(\mathbf{r}_0) = n_0 \mathbf{e}_p \cdot (\mathbf{r} - \mathbf{r}_0) = n_0 |\mathbf{r} - \mathbf{r}_0| \sin \theta_p$ , with  $\theta_p$  the zenith angle of  $\mathbf{e}_p$  to the observation direction.

If  $n_0=1$  then the optical path difference represents geometrical distance, i.e.  $\Delta z = |\mathbf{r} - \mathbf{r}_0| \sin \theta_p$ . As the surface normal vector  $\mathbf{n}_p$  subtends an angle  $\alpha_p$  to the  $z$ -axis (Eqn. (16)), then

$$\tan \alpha_p = \frac{|\mathbf{r} - \mathbf{r}_0| \sin \theta_p}{|\mathbf{r} - \mathbf{r}_0|} = \sin \theta_p \quad (19)$$

Similarly, it can be shown that the azimuth of the normal vector,  $\beta_p$ , is simply related to the azimuth of corresponding illumination vector,  $\xi_p$ , by

$$\xi_p = \beta_p + \pi \quad (20)$$

Therefore, once the normal vectors  $\mathbf{n}_p$  have been obtained for all surface reconstructions via plane fitting, the angles  $\alpha_p$  and  $\beta_p$  are obtained from Eqns. (17) and (18) and finally the illumination direction  $\mathbf{e}_p$  is determined using Eqns. (19) and (20) as

$$\mathbf{e}_p = (\sin \theta_p \cos \xi_p, \sin \theta_p \sin \xi_p, \cos \theta_p) \quad (21)$$

The sensitivity vectors of the system can now be evaluated directly using Eqn. (21) and the observation vector  $\mathbf{e}_o = (0, 0, -1)$ —see Fig. 2:

$$\mathbf{S}_p = \frac{2\pi}{\lambda_c} (\mathbf{e}_p - \mathbf{e}_o) = \frac{2\pi}{\lambda_c} (\sin \theta_p \cos \xi_p, \sin \theta_p \sin \xi_p, 1 + \cos \theta_p), \quad (22)$$

or, in matrix form:

$$\mathbf{S} = \frac{2\pi}{\lambda_c} \begin{pmatrix} \sin \theta_1 \cos \xi_1 & \sin \theta_1 \sin \xi_1 & 1 + \cos \theta_1 \\ \sin \theta_2 \cos \xi_2 & \sin \theta_2 \sin \xi_2 & 1 + \cos \theta_2 \\ \sin \theta_3 \cos \xi_3 & \sin \theta_3 \sin \xi_3 & 1 + \cos \theta_3 \end{pmatrix}, \quad (23)$$

The sensitivity and observation vectors, as evaluated from the reference surface reconstructions using Eqns. (16)-(22) are shown in the Fig. 5(c).

### 4.3. Three dimensional displacement distribution

The technique presented in this paper has been designed to measure all displacement components in the full volume of scattering materials with interferometric sensitivity. This is done by measuring changes in the 3-D phase distributions between two separate scans before and after

loading or moving the sample. By using three illumination directions it is possible to simultaneously evaluate the phase change at every point within the reconstructed volume. The relationship between the measured phase change and the displacement field can be expressed in matrix form by

$$\mathbf{\Phi} = \mathbf{S}\Delta\mathbf{r} \quad (24)$$

where  $u$ ,  $v$ , and  $w$  represent the displacements along the  $x$ ,  $y$  and  $z$  axes, respectively,  $\Delta\mathbf{r} = (u, v, w)^T$  and  $\mathbf{\Phi} = (\phi_1, \phi_2, \phi_3)^T$  ( $^T$  indicates transposed). Finally, the 3-D distribution of the displacement vector within the sample is thus obtained through inversion of the sensitivity matrix as

$$\Delta\mathbf{r} = \mathbf{S}^{-1}\mathbf{\Phi} \quad (25)$$

This operation has to be performed in a voxel by voxel basis in the reconstructed volume.

#### 4.4. Volume registration

In order to solve Eqn. (25) for each voxel in the reconstructed volume, the reconstructions associated to different illumination beams, i.e. peaks “01”, “02” and “03”, need to be ‘registered’. Registration is the process by which corresponding voxels in each reconstructed volume are brought to the same position in a common coordinate system. This usually involves a mathematical transformation that may include a combination of translation, rotation and shear in most cases. In this paper, registration requires the subtraction of the carrier frequency for each illumination direction described by the first term between squares brackets in Eqn. (15). Moreover, subtraction of the position dependent optical path difference described in the second term between square brackets in Equation (15),  $\mathbf{e}_p \cdot (\mathbf{r} - \mathbf{r}_0)$ , is also required. Fortunately, this is a

simple task once the normal vectors  $\mathbf{n}_p$  have been estimated, and can be done efficiently through a simple geometric transformation.

### 5. 3-D full-sensitivity displacement measurements

In this Section, we present experimental results on the measurement of a three dimensional displacement field within the bulk of an epoxy resin block seeded with scattering particles (titanium oxide,  $1\mu\text{m}$  average diameter) much smaller than the size of the volume point spread function (PSF) of the WSI system ( $25\ \mu\text{m}$  laterally and  $68\ \mu\text{m}$  axially). The particles/resin volume fraction was  $\sim 3 \times 10^{-3}$ , which results in  $\sim 100$  particles per PSF. If particles were sparse as required by particle image velocimetry, there would be regions in the volume that would not contribute any signal and thus no displacement information could be retrieved. On the other hand, a high volume fraction would result in **multiple scattering, which increases the noise floor and reduces the depth resolution of the system (the point spread function broadens in the axial direction). This is because of the extended optical path due to multiple scattering events, which effectively de-localises the scattering centres.**

The displacement field consists of in-plane rotation on the  $xy$ -plane (see Fig. 1) and out-of-plane tilt about the  $x$ -axis, which were introduced with a rotation and a kinematic stage, respectively. These controlled displacements are easy to implement and provide a benchmark to validate the full field measurements obtained with the WSI system. Fig. 7 shows ‘ $y\Lambda$ ’ cross sections of the registered reconstructed volumes of the sample, “01”, “02” and “03”, corresponding to each of the illumination beams. The top row shows the magnitude of the Fourier transform, whilst the bottom row shows the wrapped phase difference volumes  $\phi_1$ ,  $\phi_2$  and  $\phi_3$  obtained after rotating and tilting the sample (phase values between  $-\pi$  and  $\pi$ ). A cubic kernel of  $7 \times 7 \times 7$  voxels was

used on the terms  $\sin(\Phi)$  and  $\cos(\Phi)$  before the  $\text{atan}$  function evaluation, to reduce speckle noise. The phase volumes were then unwrapped with a 3-D path following algorithm that prevents the unwrapping path to go through phase singularity loops [31, 32]. Finally, the 3-D displacement field components  $u$ ,  $v$  and  $w$  were calculated for each voxel using Eqn. (25). The presence of some unwrapping errors in the  $\phi_1$ ,  $\phi_2$  and  $\phi_3$  phase volumes meant that only  $16 \times 35 \times 71$  ( $m, n, p$ ) voxels were obtained without unwrapping errors, corresponding to a volumetric field of view of  $\sim 0.9\text{mm} \times 0.4\text{mm} \times 0.9\text{mm}$  ( $x, y, z$ ). Fig. 8 shows cross sections of the measured average 3-D displacement field corresponding to the epoxy sample under in-plane rotation and out of plane tilt. From top to bottom, the rows indicate the displacement components  $u$ ,  $v$  and  $w$  along the  $x$ ,  $y$  and  $z$  axes, respectively. From left to right, the columns show sections of the data volume on planes  $y\Lambda$ ,  $x\Lambda$  and  $xy$ . Notice the gradient in the  $u$  and  $v$  displacement fields, as expected for an in-plane rotation around the observation direction, and the gradient of displacement  $w$  at the bottom right, which corresponds to out-of-plane tilt. In order to compare the measured displacements with the known ones introduced with the rotation and tilt stages, the  $u(x, y)$ ,  $v(x, y)$  and  $w(x, y)$  displacements shown in Fig. 8 were averaged along the  $x$ ,  $y$  and  $x$  axes, respectively, to reduce noise. In all cases an excellent agreement was observed between the ‘measured’ and ‘reference’ displacements –see Fig. 9. The root mean squared deviation between the theoretical and measured displacements  $u(x, y, z)$ ,  $v(x, y, z)$  and  $w(x, y, z)$  were, respectively,  $0.14\mu\text{m}$ ,  $0.20\mu\text{m}$  and  $32.5\text{nm}$ .

Assuming no memory constraints during image acquisition, the current WSI interferometer can generate a raw data volume of approximately  $512 \times 640 \times N_t$  (rows, columns, frames). The maximum number of frames  $N_t$  is given by the ratio of the laser frequency tuning range to the minimum frequency step:  $N_t = \Delta\nu/\delta\nu = 17.495\text{THz}/0.0002\text{THz} \sim 87,000$  frames. After re-

registration, the size of the ‘displacement’ volumes  $u$ ,  $v$  and  $w$  is reduced to  $\sim 512 \times 640 \times N_f / 24$  due to the data processing required in the Fourier domain. The factor  $1/24$  arises from the fact that  $1/2$  of the frequency axis (negative frequencies) is neglected, another  $1/2$  is lost to the autocorrelation terms, then  $1/3$  of the remaining bandwidth is used for each sensitivity vector and finally  $\sim 1/2$  of that range is effectively used to accommodate the object thickness due to the tilt in the frequency space. Thus, the reconstructed displacement volumes would contain  $\sim 512 \times 640 \times 3600$  voxels. If a  $7 \times 7 \times 7$  convolution kernel is used to reduce spatial noise then the displacement volumes would provide  $\sim 70 \times 90 \times 520$  independent measurements. The maximum ‘effective’ depth range can be estimated from Equation (12) by considering  $\delta k = 4.19 \text{m}^{-1}$  and an extra factor of  $1/12$  ( $1/2$  already taken into account by discarding negative frequencies) as  $\Lambda_{M\_eff} = \Lambda_M / 12 \sim 6.2 \text{mm}$  (6.2mm in the current setup as only 8748 frames were recorded, as explained in Section 4.1). This is assuming that multiple scattering and absorption do not set a lower limit.

## 6. Conclusion

We described a method based on wavelength scanning interferometry to measure 3-D displacement fields within scattering materials. It provides 3-D reconstructions of the material microstructure and also depth-resolved phase information that is used to evaluate all the components of the displacement vector at each voxel of the data volume, effectively extending full-sensitivity Digital Speckle Pattern Interferometry into three dimensions. The ability to measure the complete set of displacement components within the volume of the sample opens exciting opportunities in experimental mechanics, for instance the identification of constitutive parameters in anisotropic or multi-material samples. This is usually done by finite element model updating, or alternatively using the virtual fields method, two powerful inversion techniques that

require full field displacement or strain fields. Some issues that need to be investigated include the effects that material dispersion, birefringence, optical absorption, multiple scattering and surface refraction may have in the measured displacements and strains. Moreover, phase singularities can be so abundant and complex in a 3-D volume that robust 3-D phase unwrapping algorithms are required to expand the measurement volume. This technique can be viewed as frequency multiplexed OCT in which each channel carries information for a specific displacement sensitivity.

### **Acknowledgements**

The authors wish to thank EPSRC for their financial support with grant EP/E050565/1, Dr. G. E. Galizzi for his technical guidance and Prof. J. M. Huntley for his assistance with the 3-D unwrapping software.

## Figure captions

**Figure 1** WSI set-up showing the tunable laser (TL), 2×4 PLC splitter, InGaAs detector, pellicle beamsplitter (PBS), absorber plate (AP), pinhole (PH), aperture stop (AS), sample (S), lenses (L<sub>1</sub>-L<sub>7</sub>), optical fibres (OF<sub>1</sub>, OF<sub>2</sub>, OF<sub>3</sub>, OF<sub>R</sub>) and personal computer (PC).

**Figure 2** Generalized optical path diagram for WSI with multiple illumination directions for a weakly scattering material (a) and an opaque surface (b).

**Figure 3** Intensity signal recorded at one pixel during a WSI scan, when an opaque flat surface is imaged under 3-beam illumination (a); its corresponding Fourier transform, showing cross correlation terms “01”, “02” and “03” and autocorrelation terms “12”, “13” and “23” (b); peak 01 in more detail (c).

**Figure 4**  $y\Lambda$  cross-section of the magnitude of the Fourier transform volume obtained when a flat opaque surface is reconstructed, shown in reverse contrast for clarity. Lines corresponding to the auto correlation terms “12”, “23” and “13” and the cross correlation terms “01”, “02” and “03” are clearly visible. Their tilt is a consequence of the oblique illumination.

**Figure 5** Planes of best fit obtained for reconstructions “01”, “02” and “03” for a reference flat surface (a); Plane of best fit for reconstruction “01” showing its normal vector (b); and sensitivity and observation vectors, as evaluated from the reference surface reconstructions using Eqns. (16)-(22) (c).

## Figure 6

**Figure 7** Cross-sections of magnitude and the wrapped phase volumes of a weakly scattering sample that has undergone simultaneous in-plane rotation and out-of-plane tilt (phase values between  $-\pi$  and  $\pi$ ).

**Figure 8** Cross sections of the measured 3-D displacement field corresponding to a sample under in-plane rotation and out of plane tilt. The rows indicate the displacement components  $u$ ,  $v$  and  $w$  along the  $x$ ,  $y$  and  $z$  axes, respectively. The columns show sections of the data volume on planes  $y\Lambda$ ,  $x\Lambda$  and  $xy$ . Displacements units: m.

**Figure 9** ‘Measured’ (bold line) and ‘reference’ (dotted line) average displacement profiles obtained for simultaneous in-plane rotation and out-of-plane tilt of the sample.

List of figures

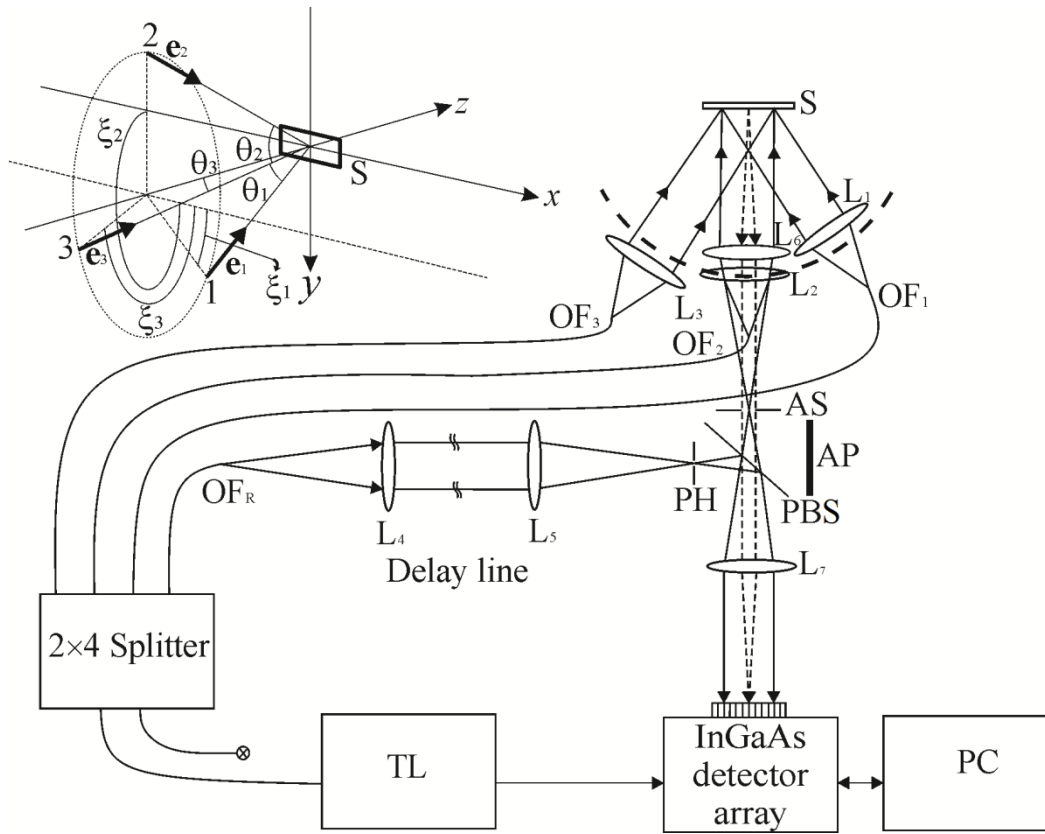


Figure 1

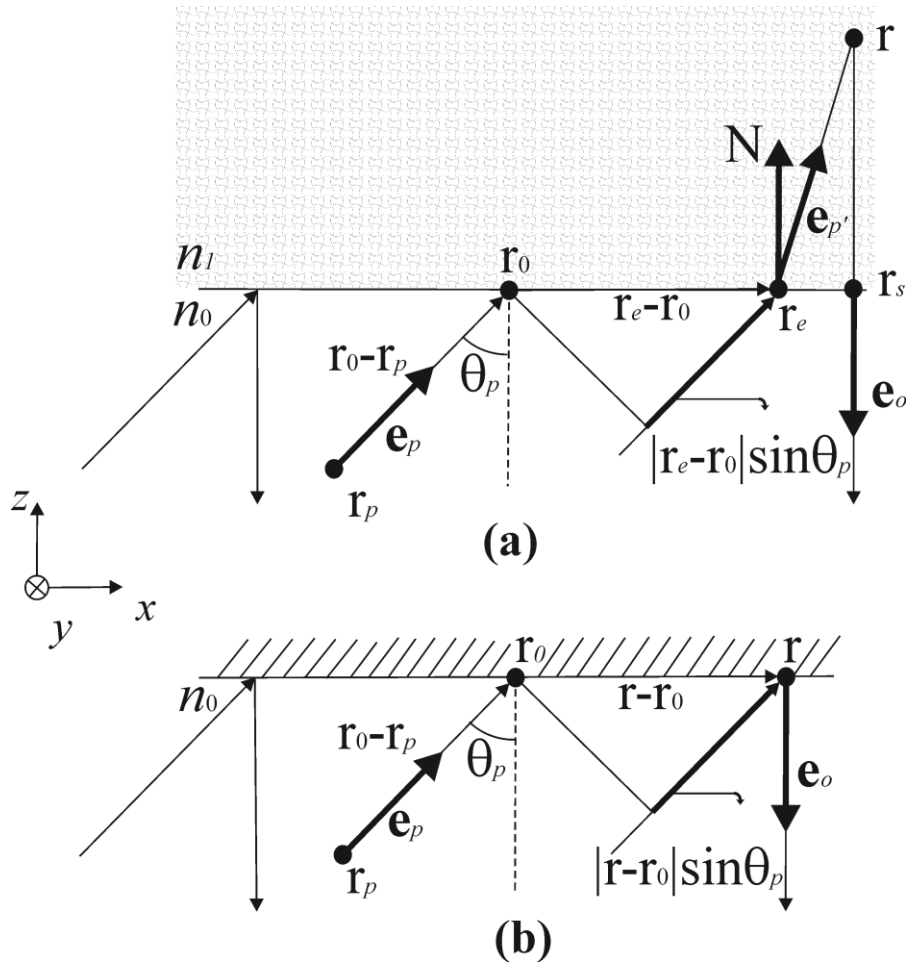
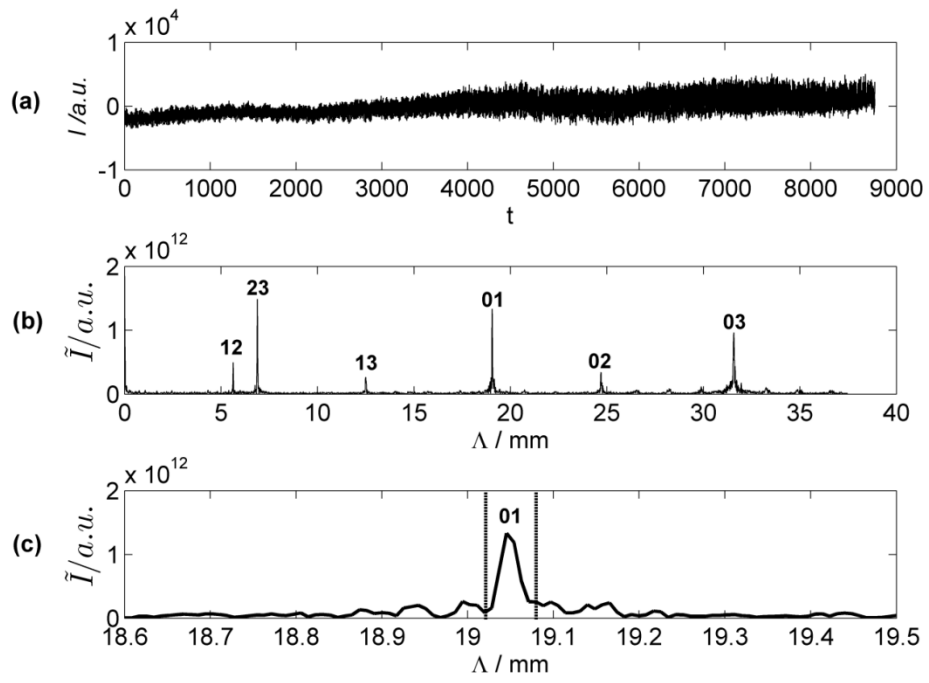
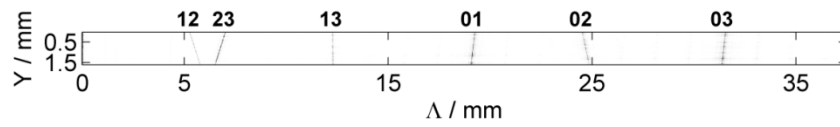


Figure 2



**Figure 3**



**Figure 4**

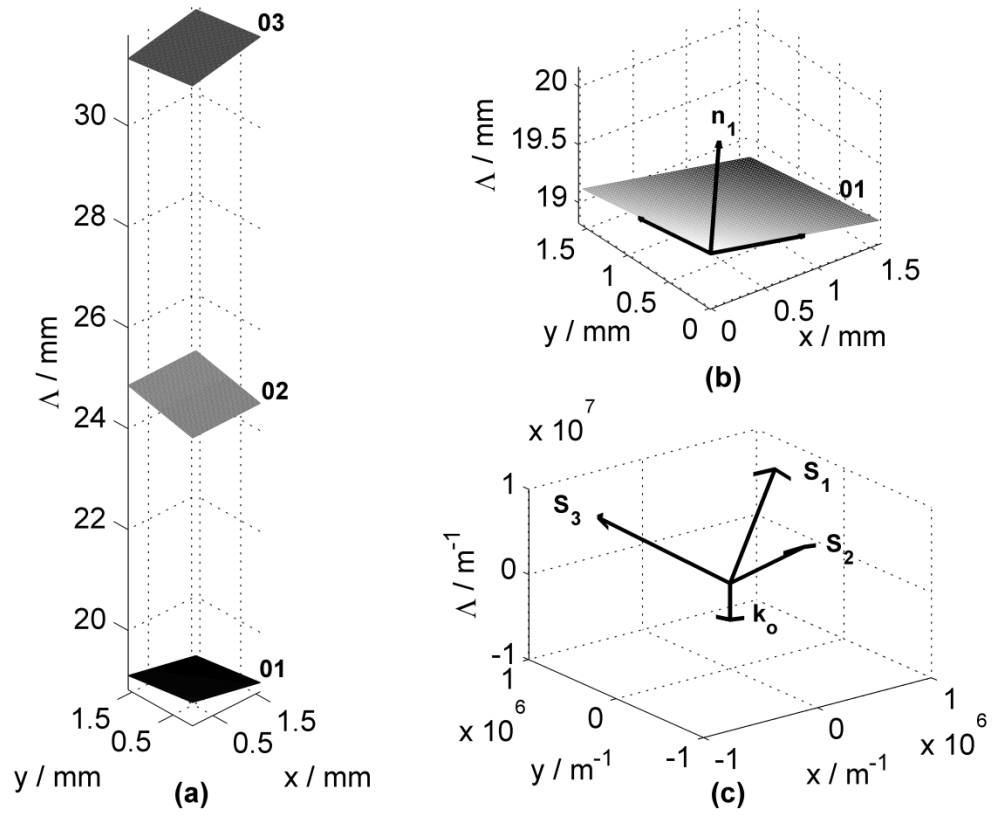
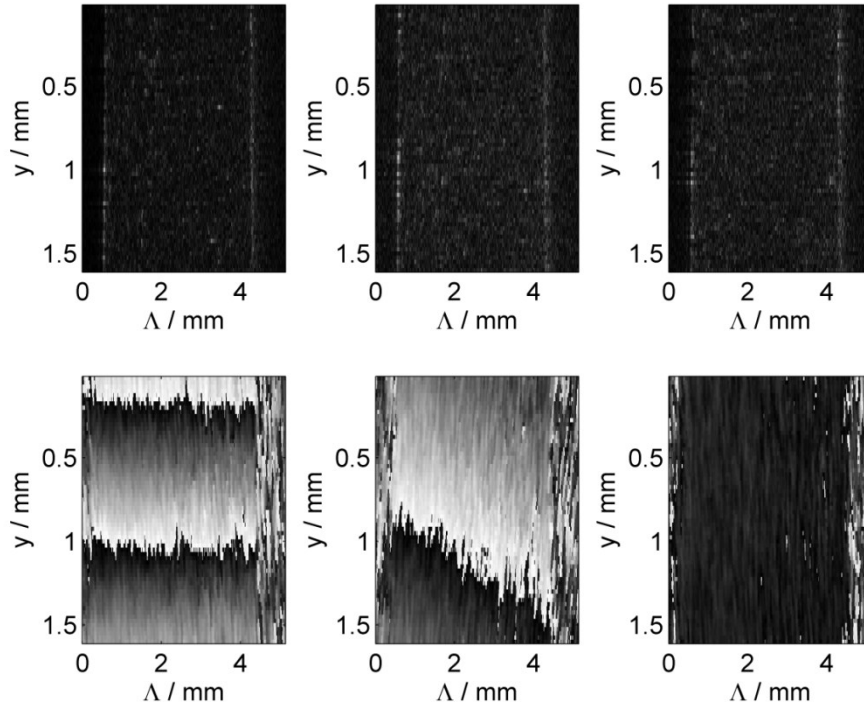


Figure 5

**Figure 6**



**Figure 7**

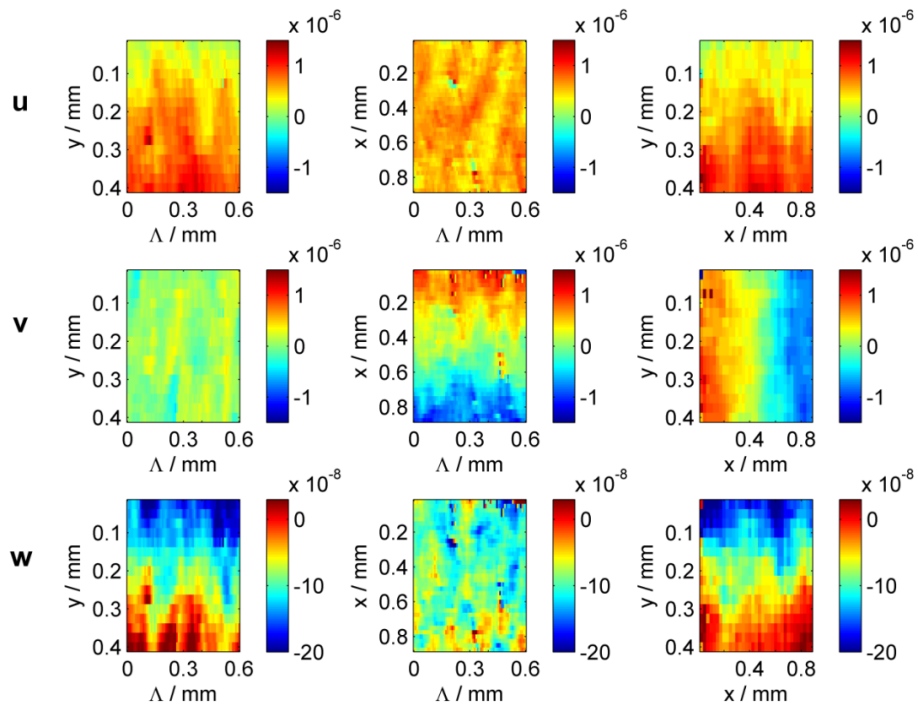


Figure 8(Gray scale picture of Figure 8 available for printed version)

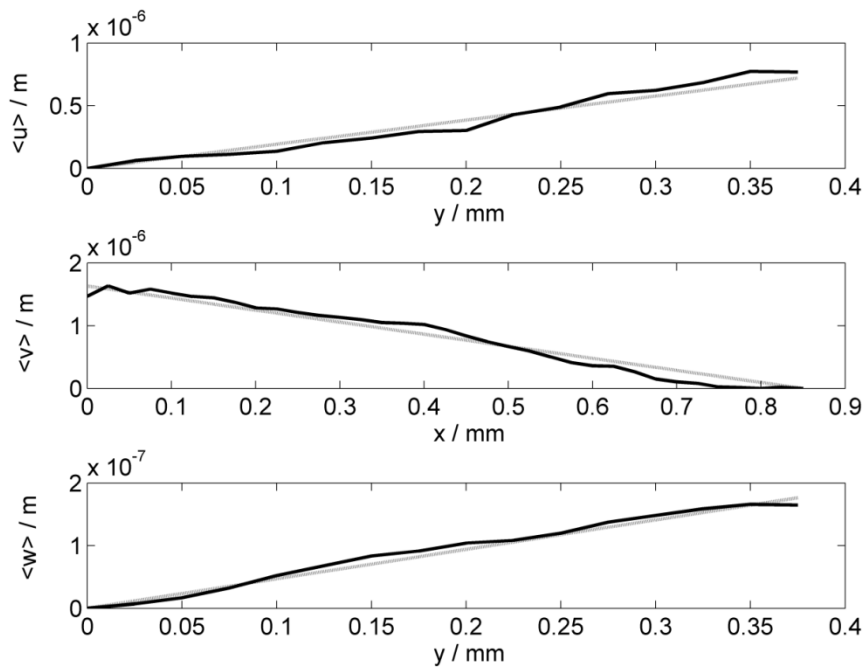


Figure 9

## References

1. S. Avril, M. Bonnet, A. S. Bretelle, M. Grédiac, F. Hild, P. Ienny, F. Latourte, D. Lemosse, S. Pagano, E. Pagnacco, and F. Pierron, "Overview of Identification Methods of Mechanical Parameters Based on Full-field Measurements," *Exp. Mech.* **48**, 381-402 (2008).
2. S. Avril, and F. Pierron, "General framework for the identification of constitutive parameters from full-field measurements in linear elasticity," *Int. J. Solids Struct* **44**, 4978-5002 (2007).
3. M. Grédiac, F. Pierron, S. Avril, and E. Toussaint, "The Virtual Fields Method for Extracting Constitutive Parameters From Full-Field Measurements: a Review," *Strain* **42**, 233-253 (2006).
4. P. D. Ruiz, F. Jumbo, A. Seaton, J. M. Huntley, I. A. Ashcroft, and G. M. Swallowe, "Numerical and experimental investigation of three-dimensional strains in adhesively bonded joints," *J. Strain Anal. Eng. Des.* **41**, 583-596 (2006).
5. I. Robinson, and R. Harder, "Coherent X-ray diffraction imaging of strain at the nanoscale," *Nat. Mater.* **8**, 291-8 (2009).
6. M. A. Sutton, J. J. Ortu, and H. W. Schreier, "Image Correlation for Shape, Motion and Deformation Measurements- Basic Concepts, Theory and Applications," (Springer, 2009).
7. B. K. Bay, "Methods and applications of digital volume correlation," *J. Strain Anal. Eng. Des.* **43**, 745-760 (2008).

8. G. E. Elsinga, F. Scarano, B. Wieneke, and B. W. van Oudheusden, "Tomographic particle image velocimetry," *Exp. Fluids* **41**, 933-947 (2006).
9. L. Liu, and E. F. Morgan, "Accuracy and precision of digital volume correlation in quantifying displacements and strains in trabecular bone," *J. Biomech.* **40**, 3516-20 (2007).
10. F. Forsberg, and C. R. Siviour, "3D deformation and strain analysis in compacted sugar using x-ray microtomography and digital volume correlation," *Meas. Sci. Technol.* **20**, 095703 (2009).
11. M. Gates, J. Lambros, and M. T. Heath, "Towards High Performance Digital Volume Correlation," *Exp. Mech.* **51**, 491-507 (2010).
12. A. Germaineau, P. Doumalin, and J. C. Dupre, "3D Strain Field Measurement by Correlation of Volume Images Using Scattered Light: Recording of Images and Choice of Marks", *Strain* **43**, 207-218 (2007).
13. Y. Han, B. Jhao, D. W. Kim, and H. J. Kwon, "Diagnosis of Breast Tumor using 2D and 3D Ultrasound Imaging," in Proceedings of the ASME 2011 International Mechanical Engineering Congress & Exposition IMECE2011, Denver, Colorado, USA, 11-17 November, (2011).
14. C. Franck, S. Hong, S. A. Maskarinec, D. A. Tirrell, and G. Ravichandran, "Three-dimensional Full-field Measurements of Large Deformations in Soft Materials Using Confocal Microscopy and Digital Volume Correlation," *Exp. Mech.* **47**, 427-438 (2007).

15. J. M. Schmitt, "OCT elastography: imaging microscopic deformation and strain of tissue," *Opt. Express* **3**, 199-211 (1998).
16. B. K. Bay, "Texture Correlation: A Method for the Measurement of detailed Strain Distributions Within Trabecular Bone," *J. Orthop. Res.*, **13**, 258 –267 (1995).
17. C. L. Gilchrist, J. Q. Xia, L. A. Setton, and E. W. Hsu, "High-Resolution Determination of Soft Tissue Deformation Using MRI and first-Order Texture Correlation," *IEEE Trans. Med. Imaging* **23**, 546-553 (2004).
18. A. K. Knutsen, Y. V. Chang, C. M. Grimm, L. Phan, L. A. Taber, and P. V. Bayly, "A new method to measure cortical growth in the developing brain," *J. Biomech. Eng.* **132**, 101004 (2010)
19. S. Avril, J. M. Huntley, F. Pierron, and D. D. Steele, "3D Heterogeneous Stiffness Reconstruction Using MRI and the Virtual Fields Method," *Exp. Mech.* 479-494 (2008).
20. D. Szotten, W. R. B. Lionheart, and R. A. Tomlinson, "Tomographic reconstruction of stress from photoelastic measurements using elastic regularization," *Inverse Prob.* (2006).
21. D. Stifter, E. Leiss-Holzinger, Z. Major, B. Baumann, M. Pircher, E. Götzinger, C. K. Hitzenberger, and B. Heise, "Dynamic optical studies in materials testing with spectral-domain polarization-sensitive optical coherence tomography," *Opt. Express* **18**, 25712-25 (2010).
22. R. K. Wang, S. Kirkpatrick, and M. Hinds, "Phase-sensitive optical coherence elastography for mapping tissue microstrains in real time," *Appl. Phys. Lett.* **90**, 164105 (2007).

23. P. Li, A. Liu, L. Shi, X. Yin, S. Rugonyi, and R. K. Wang, "Assessment of strain and strain rate in embryonic chick heart in vivo using tissue Doppler optical coherence tomography," *Phys. Med. Biol.* **56**, 7081-92 (2011).
24. P. D. Ruiz, Y. Zhou, J. M. Huntley, and R. D. Wildman, "Depth resolved whole field displacement measurement using wavelength scanning interferometry," *J. Opt. A: Pure Appl. Opt.* **6**, 679-683 (2004).
25. P. D. Ruiz, J. M. Huntley, and R. D. Wildman, "Depth-resolved whole-field displacement measurement by wavelength-scanning electronic speckle pattern interferometry," *Appl. Opt.* **44**, 3945-3953 (2005).
26. P. D. Ruiz, J. M. Huntley, and A. Maranon, "Tilt scanning interferometry: a novel technique for mapping structure and three-dimensional displacement fields within optically scattering media," *Proc. R. Soc.* (2006).
27. M. H. De la Torre-Ibarra, P. D. Ruiz, and J. M. Huntley, "Double-shot depth-resolved displacement field measurement using phase-contrast spectral optical coherence tomography," *Opt. Express* **14**, 9643-56 (2006).
28. M. H. De la Torre-Ibarra, P. D. Ruiz, and J. M. Huntley, "Simultaneous measurement of in-plane and out-of-plane displacement fields in scattering media using phase-contrast spectral optical coherence tomography," *Opt. Lett.* **34**, 806-808 (2009).

29. P. Ruiz, J. Huntley, and J. Coupland, "Depth-resolved Imaging and Displacement Measurement Techniques Viewed as Linear Filtering Operations," *Exp. Mech.* **51**, 453-465 (2011).
30. J. M. Huntley, and P. D. Ruiz, "Depth-Resolved Displacement Field Measurement," in *Advances in Speckle Metrology and Related Techniques*, G. H. Kaufmann, Ed., (Wiley-VCH, 2011), PP 37-104.
31. M. F. Salfity, P. D. Ruiz, J. M. Huntley, M. J. Graves, R. Cusack, and D. A. Bearegard, "Branch cut surface placement for unwrapping of undersampled three-dimensional phase data: application to magnetic resonance imaging arterial flow mapping," *Appl. Opt.* **45**, 2711-22 (2006).
32. O. Marklund, J. M. Huntley, and R. Cusack, "Robust unwrapping algorithm for three-dimensional phase volumes of arbitrary shape containing knotted phase singularity loops," *Opt. Eng.* **46**, 085601 (2007).